Thermochromic Aggregation-Induced Dual Phosphorescence via Temperature-Dependent *sp*^{3}-Linked Donor-Acceptor Electronic Coupling

Tao Wang[1]*, Zhubin Hu*[2]*, Xiancheng Nie*[1]*, Linkun Huang*[1]*, Miao Hui*[1]*, Xiang Sun*[2,3*] *& Guoqing Zhang*[1*]

[1]*Hefei National Laboratory for Physical Science at the Microscale, University of Science and Technology of China, Hefei, China, 230026.*

[2]*Division of Arts and Science, NYU-ECNU Center for Computational Chemistry, NYU Shanghai, Shanghai, China, 200122.*

[3]*Department of Chemistry, New York University, New York, USA, 10003.*

ABSTRACT. Aggregation-induced emission (AIE) has proven to be a viable strategy to achieve highly efficient RTP in bulk by restricting molecular motions. Here we show that by utilizing triphenylamine (**TPA**) as an electronic donor which connects to an acceptor via an *sp*^{3} linker, six **TPA**-based AIE-active RTP luminophores were obtained. Distinct dual phosphorescence bands emitting from largely localized donor and acceptor triplet emitting states, respectively, could be recorded at lowered temperatures; at room temperature, only a merged RTP band is present. Theoretical investigations reveal that the two temperature-dependent phosphorescence bands both originate from local/global minima from the lowest triplet excited state (T_1). The reported molecular construct serves as an "intermediary case" between a fully conjugated donor-acceptor

system and a donor/acceptor binary mix, which may provide important clues on the design and control of high-freedom molecular systems with complex excited-state dynamics.

Suppressing nonradiative decays (e.g., intramolecular motions) and promoting the intersystem crossing rate (ISC) are crucial to realize organic room-temperature phosphorescence (RTP) intense enough for practical applications[1,2]. Up till now, several RTP design principles have been proposed, such as introducing bulky hindrance groups[3,4] and spiro linkers[5], constructing aggregates[6-8], polymers[9,10] and self-assemblies[11-13], host-guest[14-16] and bonding[17-19] interactions, as well as tuning charge-transfer (CT) states[20,21]. Recently, we put forward a new RTP design principle based on an sp^3-linker connected donor-acceptor dyad, where an angled intramolecular CT state is believed to enhance spin-orbit coupling due to electron circular motion during transition[22,23]. For example, a proton-activated "off-on" RTP molecular probe could be developed based on this principle[22]. However, most RTP emitters still require stringent environmental factors such as low temperature, solid matrix assistance, and/or oxygen exclusion, which can be rather cumbersome for practical applications. Since 2001[24], aggregation-induced emission (AIE) luminophores have been a research hotspot because of their enormous potentials in solid-state display[25-27], bio-probes[28-30], circularly polarized luminescence[31,32], and "on-off" sensors[33], with an advantage being "emitting in their own microenvironments". Therefore, a universal design method for the development of RTP materials may be built upon less environmental-sensitive AIE core structures with RTP's increasing use in chemical sensing[34,35], data storage[36,37], bioimaging[38,39] and OLEDs[40,41]. Herein, we present an RTP design strategy of molecular solids by combining the concept of AIE and the donor-sp^3 linker- acceptor dyad molecular motif and demonstrate that such a design yields an unexpected phenomenon of thermochromic phosphorescence (TCP). We also show that the temperature-dependent emission is largely dictated by *how strongly* the two largely locally excited triplet emitting states (i.e., donor triplet ^3LE_D and acceptor triplet ^3LE_A) associate (Figure 1a). The **TPA** moiety was selected as an AIE activator as well as an electron donor with the acceptor varying in chemical structures. Shown in Figure 1b, five **TPA**-functionalized AIE-active RTP molecules were synthesized via simple Suzuki-Miyaura or Ullmann-type coupling reactions and the AIE properties of **TPA1-5** were investigated.

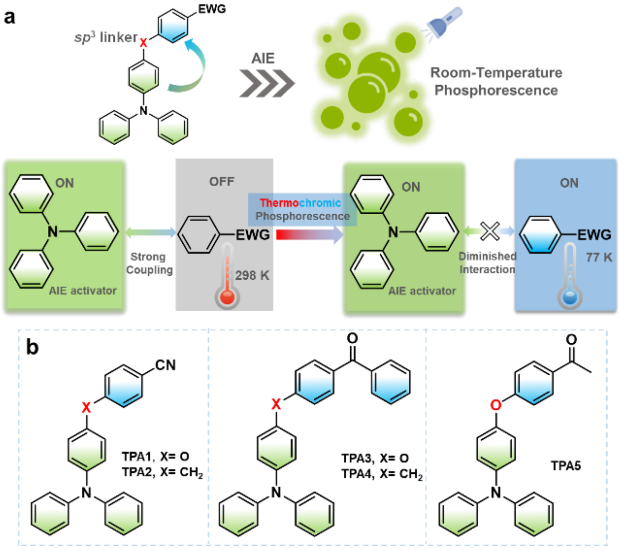

Figure 1. AIE-active dual-phosphorescence molecular design. **a** Design concept of AIE-gen donor-*sp*^{3} linker-acceptor thermochromic dual phosphorescent dyad via temperature-dependent coupling between two emissive triplet excited states. **b** Related chemical structures. Abbreviation: EWG = electron-withdrawing group.

Results

AIE characterization. In solution, absorption spectra conducted in THF (Figure 2a) are consistent with calculations by the time-dependent density functional theory (TD-DFT) method with the optimally tuning range-separated functional (LC-ωPBE*) and the TZVP basis set[42,43]. According

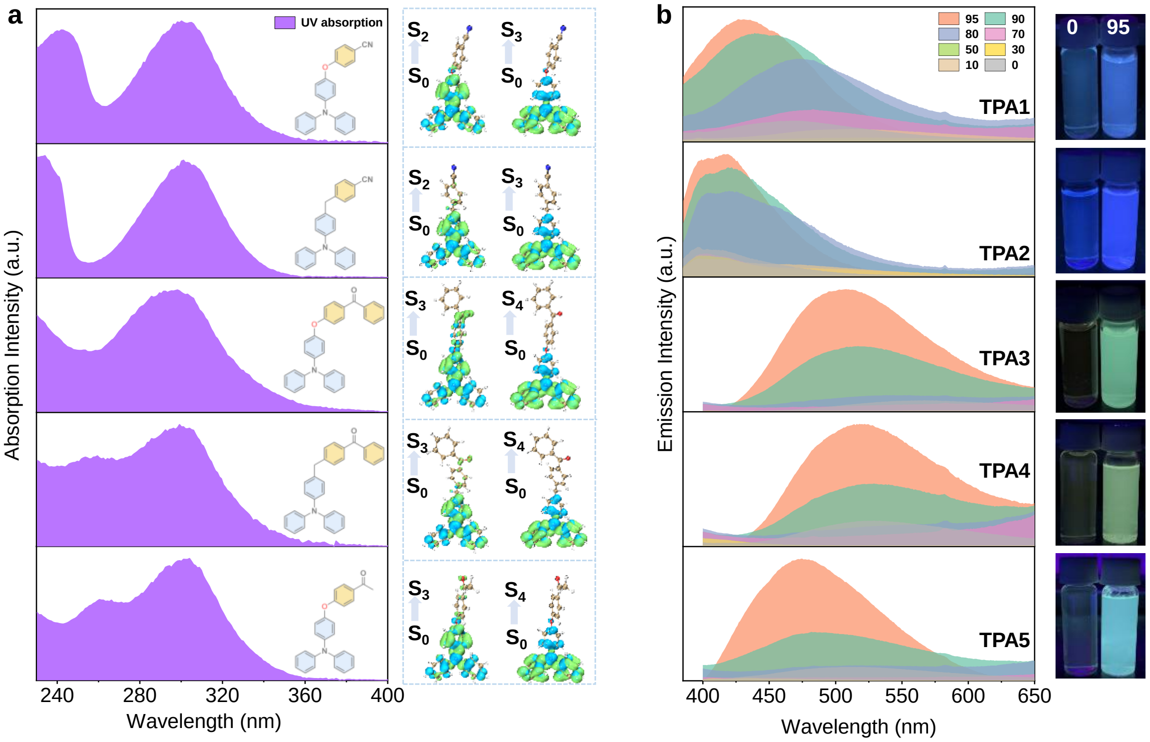

Figure 2. AIE investigations. a Normalized absorption spectra (left) of **TPA1-5** in optically dilute THF solutions and corresponding hole (blue)-electron (green) distributions (right) calculated based on the TD-DFT method. **b** Steady-state emission spectra of **TPA1-5** in a bicomponent solution mixture showing the AIE process with different THF/water ratios (0-95%, v/v) and related AIE photos under a hand-held UV lamp (water fraction: 0 and 95%, **TPA** concentration: 2.0 $\times 10^{-3}$ mol/L).

to the theoretical results (Supplementary Figure 1 and Supplementary Table 1), the reddest absorption band (>280 nm) of **TPA1-2** is mainly contributed by the second and the third singlet excited states (S_2 and S_3), while that of **TPA3-5** is dominated by S_3 and the fourth singlet excited state (S_4). The hole-electron distribution analysis performed by Multiwfn 3.7 (dev) program[44] indicates that lower electronic transitions of all **TPA**s are mainly contributed by local excitations (Figure 2a, right), and the lowest singlet excited state (S_1) is a dark state with a strong CT character, consistent with weak absorption trailing into the near UV region. The fact that the absorption maxima in various solvents exhibit almost no difference also indicates the main bands belong to transitions to localized excited states (e.g., S_2 and S_3, Supplementary Figure 2). Therefore, it can be inferred that **TPA**s are non-emissive due to a combination of excited-state energy dissipation via intramolecular rotation (propeller-shaped **TPA** moiety) and a lowest forbidden CT pathway. With increasing water fraction, a typical AIE process (Figure 2b) can be observed due to restriction of intramolecular motions and possibly newly emerged, lowest emissive states as aggregates. It has to be noted that the observed emission maximum shift mainly results from the change of mixture solvent polarity[45]. Moreover, all **TPA** aggregates in THF/water (5/95, v/v) contain long-lived emissions, and the afterglow can even be observed for certain (e.g., **TPA1)** aggregates (Supplementary Figure 3). The scanning electron microscopy (SEM) images (Supplementary Figure 4) show that some of these aggregates are in fact ordered and form nanocrystals (**TPA1**, **TPA2** and **TPA5**); the increased particle sizes of **TPA3** and **TPA4** may originate from reduced intermolecular interactions given that they exhibit high molecular complexity.

To assist further understanding of their AIE behaviours, single-crystal measurements of **TPA1** and **TPA3-5** were conducted to investigate the origin of the emission, except for **TPA2** which always generates polycrystals. As shown in Figure 3, the donor and acceptor moieties of **TPA**s adopt a highly twisted conformation due to the separation by an sp^3 linker (O or CH_2), resulting in a twist angle within a range of ~110-120°. As expected, the combined effect of a propeller-shaped **TPA** donor and an additional twist exerted by the sp^3 linker is apparent: it makes π-π stacking essentially non-existent while suppressing various molecular motions as aggregates, which is a typical AIE mechanism.

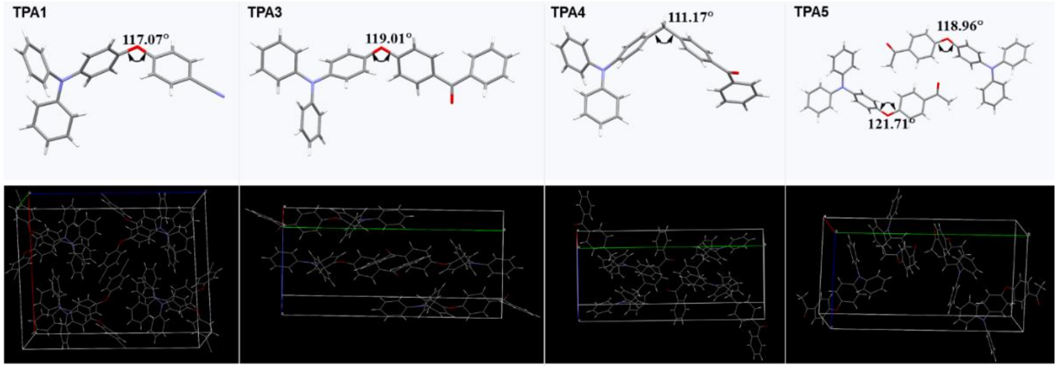

Figure 3. Single-crystal XRD analysis. Stick models (top) of **TPA1** and **TPA3-5** obtained from single-crystal XRD measurements and packing diagrams shown in wireframe model (bottom) indicating no obvious strong π-π intermolecular interactions in the solid state.

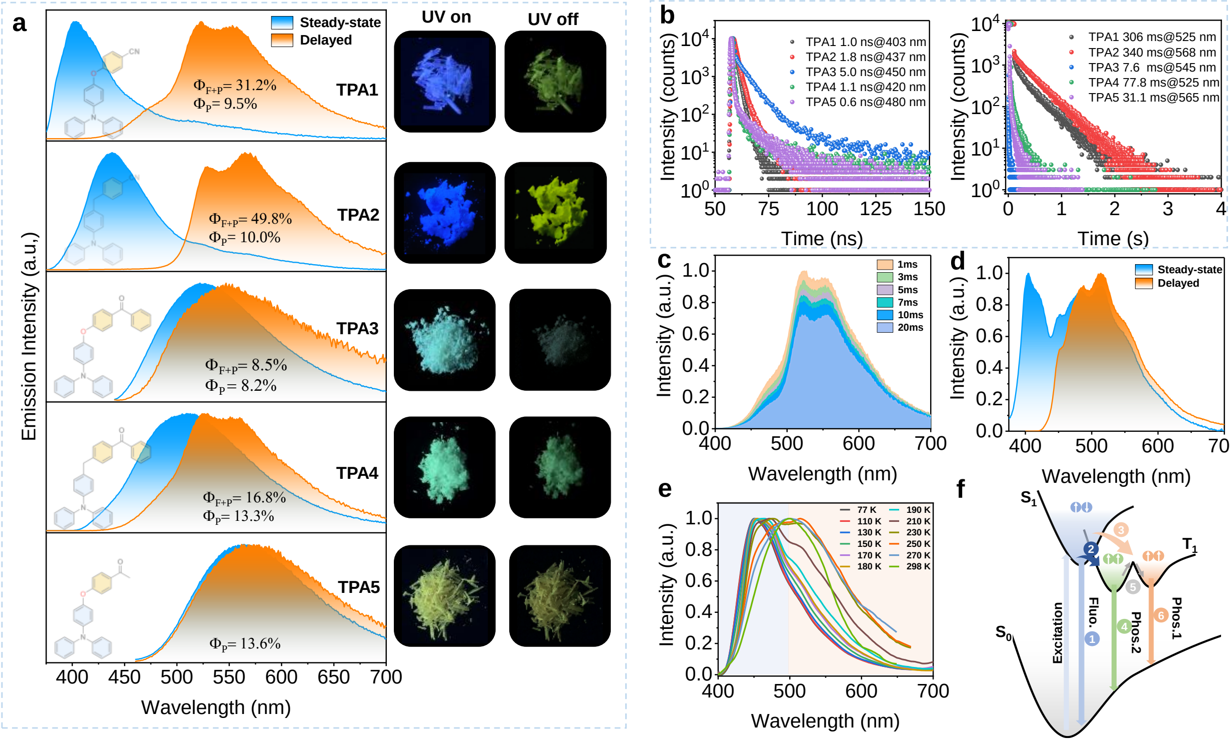

Figure 4. Photophysical investigations for TPA1-5 molecular solids. **a** Normalized emission spectra of **TPA1-5** in air at room temperature (excitation: 365 nm for **TPA1**, **TPA2** and **TPA4**; 430 nm for **TPA3**; 450 nm for **TPA5**) and corresponding photos showing **TPA1-5** excited by 365-nm UV light. **b** Time-resolved decay profiles of **TPA1-5** in air at room temperature (right:

fluorescence; left: RTP). **c** Time-resolved emission spectra of **TPA1**. **d** Normalized emission spectra of **TPA1** at 77 K. **e** Normalized phosphorescence emission spectra of **TPA1** dissolved in PMMA film (excitation: 375 nm; concentration: 3%, w/w) at different temperatures. **f** Schematic illustration of the ternary emission process; process 1: fluorescence; process 2: intersystem crossing at 77 K and 298 K; process 3: favoured intersystem crossing at 298 K; process 4&6: phosphorescence; process 5: thermal activated conformation transformation.

Photophysical properties in the aggregation state. These collected aggregates were then investigated by both steady-state and delayed luminescence spectroscopy. The optimal excitation wavelengths were assessed from solid-state UV-vis absorption and excitation spectra (Supplementary Figure 5). For **TPA1** and **TPA2**, the steady-state emission exhibits a main AIE-fluorescence band (λ_{em} = 403 and 437 nm, respectively, Figure 4a) with nanosecond lifetimes (Figure 4b, left). A low-energy band over 500 nm with a lifetime of >300 ms (Figure 4b, right) is presumably due to the AIE-RTP. When the delayed spectrum of **TPA1** was examined, we observed a high energy broad shoulder (~485 nm) that is >1600 cm^{-1} above from lowest triplet excited state emission (T_1). To shed light on the origin of this shoulder peak, time-resolved emission spectra were collected (Figure 4c), where the shoulder peak intensity decays faster vs. that of the main RTP peak at room temperature (Supplementary Figure 6 and 7a). At 77 K, the steady-state and delayed emissions show a tremendous increase in the shoulder band (Figure 4d), which perhaps indicates a second emissive triplet state[2]. For delayed emissions, the relative intensity ratio between the shoulder band and the main peak maintains constant (Supplementary Figure 8). This temperature-dependent phosphorescence decay kinetics suggests that the second emissive triplet excited state is feeding the lowest T_1 at room temperature, whereas the communication is cut off at 77 K.

To exclude the influence of ground-state aggregation and trace impurity contamination (which can be significant in molecular solids), the phosphorescence spectra ($\Delta t = 1$ ms) of single-crystal purity **TPA1** dissolved in PMMA were also recorded at various temperatures, where a consistently blue-shifted trend could be noted with decreasing temperature (Figure 4e), further indicative of such a second triplet state being separated from the lowest T_1. Visually, a colour change from green to sky blue in the afterglow could be noted. A schematic illustration for explaining this ternary emission (fluorescence and dual phosphoresce) is presented in Figure 4f. For highest twisted molecules with many vibrational and rotational freedoms like these **TPA** derivatives, we anticipate a very rough potential energy surface (PES) in the T_1 state: more than one local minima can therefore become the emitting states. It is reasonable to assume that a molecular geometry further away from the equilibrium position gives off emission at a longer wavelength, which is designated as T_1^L; the other emitting state closer to equilibrium position is denoted as T_1^H (L/H stands for low/high). The temperature dependency can therefore be interpreted as: 1) a higher temperature produces hotter excitons that may prefer intersystem crossing (ISC) favourable for relaxation to the T_1^L site and vice versa; 2) communications among these emitting states at local minima by thermal motions (e.g., vibrations) may be cut off at frigid temperatures, so that more distinct separation in spectrum could be revealed.

For **TPA2** aggregates, although little to no T_1^H emission band is presented at room temperature (Figure 4a and Supplementary Figure 9), a new peak shows up in the low-temperature phosphorescence spectrum (LTP, 77 K, Supplementary Figure 10) at 455 nm in addition to the main band (λ= 525 nm), indicating a higher energy barrier between the two emitting states when the CH_2 linker replaces O at room temperature. Similarly, when **TPA2** was molecularly dissolved in the PMMA film, a much stronger high energy shoulder peak (λ= 440 nm) gradually emerged

(Figure 5a) compared to the aggregated state. The experimental data above appear to indicate that two T_1 states communicate at room temperature both intermolecularly and intramolecularly, since the aggregates tend to give a much weaker T_1^H phosphorescence band irrespectively of the temperature, compared to discrete molecules in PMMA.

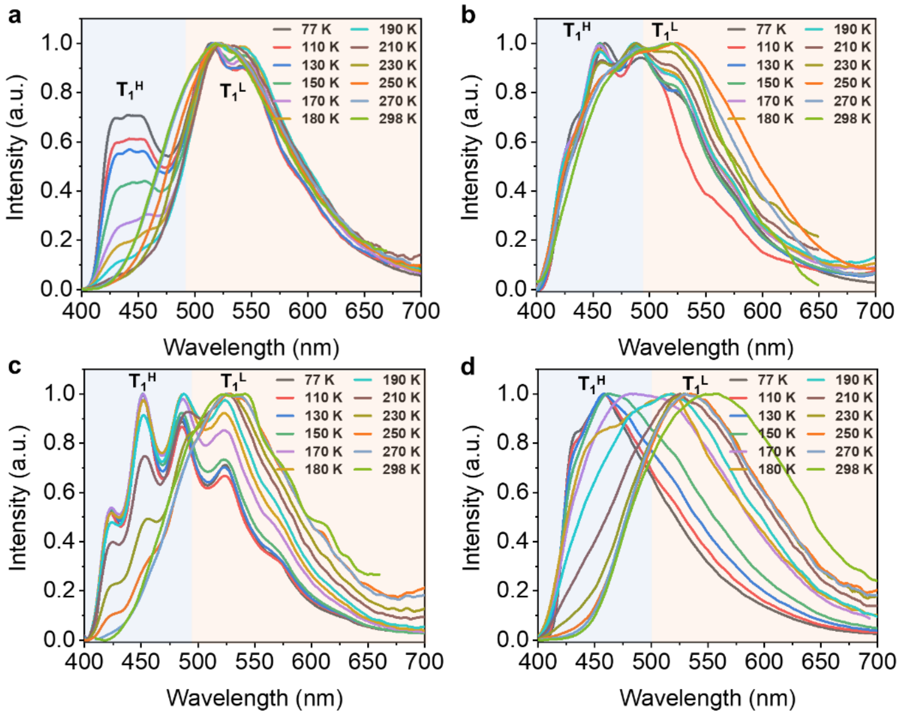

Figure 5. Temperature-dependent time-resolved emissions of PMMA films for showing dual phosphorescence. Normalized phosphorescence emission spectra of **TPA2** (**a**), **TPA3** (**b**), **TPA4** (**c**) and **TPA5** (**d**) dissolved in PMMA film (Δt = 1 ms; excitation: 375 nm; concentration: 3%, w/w) at different temperatures showing the two triplet-state emissions.

At this stage, we speculate that the T_1^L state is a **TPA**-localized triplet state with T_1^H being an acceptor (cyanobenzene) centric triplet one. To verify the hypothesis, two important experiments were conducted: 1) **TPA3** to **TPA5** with an aromatic ketone acceptor were prepared. It is well-known that benzophenone exhibits a prominent ^{3}n-π* state[46,47] with a characteristic vibrational progression in the phosphorescence spectrum separated by ~1300-1600 cm^{-1}. Indeed, such spectroscopic patterns from the T_1^H state characteristic of benzophenone ^{3}n-π* were unambiguously obtained (Figure 5b and 5c) when the temperature is reduced to or below 200 K for the two samples dissolved in PMMA films (particularly for the CH_2-linked **TPA4** where no oxygen conjugation interferes with the vibration), further revealing that phosphorescence emissions consist of two emissive triplet states from benzophenone and **TPA** subunits, respectively. It has to be noted that below 150 K, the T_1^L state appears largely suppressed, again suggesting preferential ISC relaxations at different temperatures (Figure 4f).

For **TPA5**, the 4-oxygen substituted acetophenone acceptor is expected to exhibit a mixed ^{3}π-π* and ^{3}n-π* band for T_1^H in PMMA at 77 K (λ_{em}= 455 nm) (Figure 5d). Temperature-dependent excitation spectra (Supplementary Figure 11) of **TPA1-5** dissolved in PMMA films also suggest the existence of two different emissive triplet states. In the aggregated states, all three samples (**TPA3-5**) exhibit a broad RTP emission dominated by T_1^L (Figure 4a) and much shorter RTP lifetimes (Figure 4b, Supplementary Table 2) due to strong electronic coupling between the **TPA**-localized ^{3}π-π* and the ketone-localized ^{3}n-π* state; such coupling is also present, albeit weak, at 77 K based on the phosphorescence spectra (Supplementary Figure 12-14). Notably, due to the introduction of the carbonyl group in **TPA3-5**, the fluorescence emission almost totally turns into RTP because of a promoted ISC process, and the fluorescence emission can only be measured before 480 nm (Figure 4b, left). A binary molecular mixture between **TPA** and the benzophenone precursor at 1:1 ratio was used to repeat the same experiment (Supplementary Figure 15), where it was found that the 1:1 physical mixture generates RTP bands belonging to the two molecules irrespective of the temperature. The results not only suggest that the two RTP bands do originate from the donor and acceptor, respectively, but also point to the importance of the *sp*^{3} chemical linker: *cutting off communications at low temperature but not high temperature, something completely different from blending*.

Computational investigation on the origin of dual phosphorescence. To further back the proposed T_1^H-T_1^L dual phosphorescence states model, we first selected **TPA1** as example to carry out a series of theoretical calculations via TD-DFT at the LC-ωPBE*/TZVP level in the gas state, which mimics the state of monomers in PMMA. The calculated energy diagram of the vertical excitation and spin-orbit coupling constants reveals multiple ISC channels from S_1 to a higher triplet state during RTP generation (Supplementary Figure 16), pointing to the possibility of preferential ISC channels depending on temperature. Moreover, the vertical emission calculations demonstrate that 1) the S_1 state is almost degenerate with the acceptor T_2 state, which boosts the ISC process, and 2) the energy gap between T_1 and T_2 states is relatively large (Supplementary Figure 17). However, according to the energy gap law for internal conversion[48]: $\log(k_{IC}) \approx 12-2\Delta\nu$, where k_{IC} (s^{-1}) is the internal conversion rate and $\Delta\nu$ (μm^{-1}) is the wavenumber difference between T_1 and T_2, the calculated k_{IC} for **TPA1** is $\sim 3.95\times10^{-10}$ s^{-1}, which indicates that triplet excitons can only emit as photons from T_1.

To shed light on the origin of dual phosphorescence, we further conducted relative Gibbs free energies and the three global/local-minima geometries (T1-1 to T1-3) of T_1-state **TPA1 (**Figure 6**)**. As Figure 6 shows, there are different **TPA1** conformations showing different T_1 states, which exhibit T_1 emissions contributed by donor and acceptor. Due to the existence of energy barriers (TS1 and TS2), the conformation transformation should be decided by transition energy, which can be compensated at room temperature while inhibited at low temperature, such as 77 K. T_1^H and T_1^L are not completely localized on donor and acceptor of **TPA1** perhaps because cyanobenzene is a type of extremely weak emitter, which is consistent with spectroscopic evidence that **TPA1** T_1^L emission is always dominant. Therefore, we further conducted the calculations of **TPA4**, where benzophenone is a better emitter than cyanobenzene. As anticipated, two T_1 species are localized on **TPA** and benzophenone subunits, perfectly corresponding with the experimental results (Figure 5c and S14). Therefore, we can conclude that the dual phosphorescence mainly originates from T_1 states of **TPA** derivatives in specific conformations, lining up with the dual-phosphorescence model in Figure 4f.

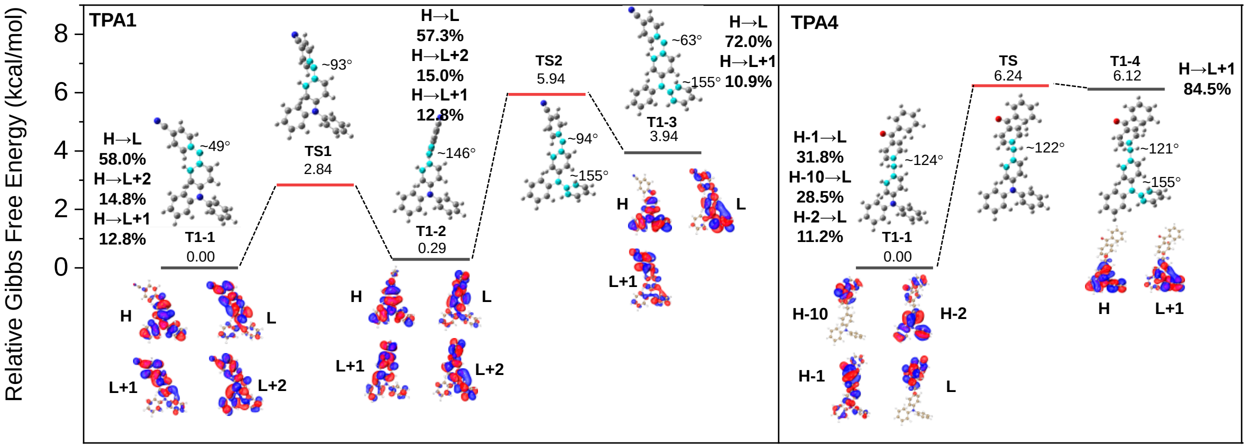

Figure 6. Theoretical computations on the conformations and molecular orbital transitions for dual phosphorescence. Calculated relative Gibbs free energies and global/local-minima geometries (T1-1, T1-2, T1-3 and T1-4) of T_1-state, the related transition states (TS) between these geometries, the optimal geometries with dihedrals of highlighted atoms, and main molecular orbital transition contributions for T_1 emissions (>10%) (H= HOMO, L=LUMO).

Application explorations. Finally, to showcase the application value of the AIE thermochromic dual phosphorescence molecules, we synthesized **TPA6** with a **TPA** donor and a pyridine acceptor (Figure 7a). The rationale is that the electron-withdrawing pyridyl group is smaller than cyanobenzene which should yield an even more separated T_1^H and T_1^L energy gap to make the visual phosphorescence colour change more dramatic and spectroscopically more resolvable. Meanwhile, the lone pair electron in the pyridine moiety is likely to make molecular stacking even more difficult in the solid state, so that no PMMA matrix is needed for the **TPA6**-based phosphorescence sensing module. Figure 7b shows that the **TPA6** solid exhibits a fluorescence emission at 425 nm (τ= 0.7 ns). Meanwhile, an obvious afterglow can be observed by the naked eye and an RTP emission band can be collected at 550 nm with a lifetime of 83 ms in air at room temperature. As the temperature decreases, a new phosphorescence band (T_1^H) appears with an emission maximum at 455 nm in the steady-state emission spectrum (Figure 7c), which can be used as a ratiometric phosphorescence/fluorescence (P/F) sensing scheme (Figure 7d) demonstrated in many previous reports.[49,50] However, here we show for the first time that a delayed spectrum can further become sensitive to an external stimulus and responds to temperature change dramatically (Figure 7e and 7f), which could be potentially used as the thermometer for indicating extremely low-temperature environment.

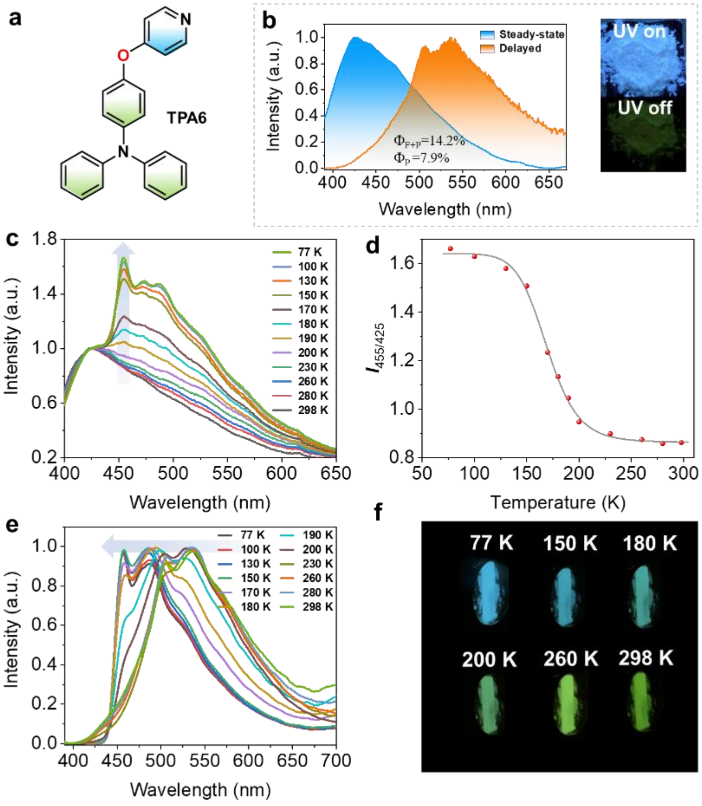

Figure 7. Photophysical properties of TPA6. a Chemical structure of **TPA6**. **b** Normalized steady-state and RTP emission (Δt = 3 ms) spectra of **TPA6** in air at room temperature; inset: photo showing **TPA6** solid excited by 365-nm UV light. **c** Relative steady-state emission spectra of **TPA6** at different temperatures. **d** Relationship between the emission intensity ratio of 455 and 425 nm (I_{455}/I_{425}) and temperature. **e** Normalized temperature-dependent phosphorescence emission spectra of **TPA6**. **f** Image showing delayed emission (> 50 ms) colour change at different temperatures.

Discussion

In summary, by introducing a **TPA**-based AIE-gen into the donor-*sp*^{3} linker-acceptor structure, several ternary emissive AIE-active RTP molecules with prompt fluorescence and dual phosphorescence were obtained. The phenomenon is explained by the presence of a **TPA**-localized T_1^L state, which couples to a higher acceptor T_1^H state at room temperature but cuts the electronic coupling off at lowered temperatures. Therefore, a universal principle for designing a dual-phosphorescence thermochromic material can be deduced and demonstrated. The current strategy benefits design for single-component, dual-phosphorescence-based molecular probes. More importantly, we expect many more structurally different molecular can be used in this strategy with a possibility of generating more than two phosphorescence bands to obtain kinetically more complex molecular systems.

Methods

Synthesis. TPA1-6 were synthesized by Suzuki-Miyaura and Ullmann-type coupling reactions. Further detailed information on synthetic procedures is provided as Supporting Information.

Measurements. ^{1}H NMR (400 MHz) spectra were collected on Bruker AV400 NMR spectrometer and operated in the Fourier transform mode at 298 K. The related chemical shifts were reported as values in ppm relative to tetramethylsilane (TMS, δ= 0) in deuterated solvents. High-resolution mass spectra (HRMS) were conducted on an Atouflex speed mass spectrometer using the electrospray ionization (ESI) mode. Single-crystal data were collected from a XtaLAB AFC12 (RINC): Kappa single diffractometer. The crystal was kept at 293 K during data collection. Using Olex2[51], the structure was solved with the ShelXT structure solution program using intrinsic phasing[52] and refined with the ShelXL refinement package using least-squares. The morphologies of the aggregates in THF/H2O (5/95, v/v) were investigated via field-emission scanning electron microscopy (FESEM, JEOL JSM-6700F, 10 kV). UV-vis spectra were measured in THF on Agilent Cary 60 UV-vis spectrometer ranging from 190- 1100 nm and data processed on Origin 2020. Steady-state and time-resolved photoluminescence emission spectra were conducted on a FluoroMax-4 spectrofluorometer (Horiba Scientific) and analyzed by Origin 2020 software. Absolute quantum yields were determined using an integrating sphere. Emission lifetime decay profiles were collected on Horiba Ultima time-resolved fluorescence spectrometer with 1MHz lasers, and the related data were analyzed with DataStation v6.6 (Horiba Scientific).

Data Availability. All relevant data that support the findings are available within this article and supporting information and are also available from authors upon reasonable request. The Crystallographic data for **TPA1**, **TPA3**, **TPA4**, and **TPA5**, have been deposited in the Cambridge Crystallographic Data Center (CCDC) (https://www.ccdc.cam.ac.uk/structures/) under accession numbers CCDC: 2022517,2022518,2022520, and 2022519.

Corresponding Author

X. Sun: xiang.sun@nyu.edu

G. Zhang: gzhang@ustc.edu.cn

Author Contributions

T. W. and G. Z. conceived and designed the project. T. W. synthesized all the related target compounds. T. W., X. N. and L. H. and H. M. performed the relevant photophysical measurements. Z. H. and X. S. conducted the theoretical calculations. T. W. and G. Z. wrote and revised the manuscript. All authors discussed the results and commented on the manuscript.

Acknowledgment

We would like to thank the National Key R&D program of China (2017YFA0303500 to G. Z.) and the National Natural Science Foundation (21975238 to G. Z. and 21903054 to X.S.). We are extremely grateful for the invaluable discussion with Prof. Yi Luo from USTC.

Competing interests

The authors declare no competing interests.

References

1. Lewis, G.N. & Kasha M. Phosphorescence and the triplet state. *J. Am. Chem. Soc.* **66**, 2100-2116 (1944).
2. Zhao, W. *et al.* Rational molecular design for achieving persistent and efficient pure organic room-temperature phosphorescence. *Chem* **1**, 592-602 (2016).
3. Ward, J. S. *et al.* The interplay of thermally activated delayed fluorescence (TADF) and room temperature organic phosphorescence in sterically-constrained donor–acceptor charge-transfer molecules. *Chem. Commun.* **52**, 2612-2615 (2016).
4. Wang, J. *et al.* Mechanoluminescence or Room-Temperature Phosphorescence: Molecular Packing-Dependent Emission Response. *Angew. Chem. Int. Ed.* **131**, 17457-17462 (2019).

5. Zhu, X. -D. *et al.* Incorporating a tercarbazole donor in a spiro-type host material for efficient RGB phosphorescent organic light-emitting diodes. *J. Mater. Chem. C* **7**, 6714-6720 (2019).
6. An, Z. *et al.* Stabilizing triplet excited states for ultralong organic phosphorescence. *Nat. Mater.* **14**, 685-690 (2015).
7. Ni, F. *et al.* Organic emitter integrating aggregation-induced delayed fluorescence and room-temperature phosphorescence characteristics, and its application in time-resolved luminescence imaging. *Chem. Sci.* **9**, 6150-6155 (2018).
8. Weng, T. *et al.* A fluorescence-phosphorescence-phosphorescence triple-channel emission strategy for full-color luminescence. *Small* **16**, 1906475 (2020).
9. Li, Q. & Li, Z. Molecular packing: another key point for the performance of organic and polymeric optoelectronic materials. *Acc. Chem. Res.* **53**, 962-973 (2020).
10. Ma, X., Xu, C., Wang, J. & Tian, H. Amorphous pure organic polymers for heavy-atom-free efficient room-temperature phosphorescence emission. *Angew. Chem. Int. Ed.* **130**, 11020-11024 (2018).
11. Ma, X., Wang, J. & Tian, H. Assembling-induced emission: an efficient approach for amorphous metal-free organic emitting materials with room-temperature phosphorescence. *Acc. Chem. Res.* **52**, 738-748 (2019).
12. Kuila, S. *et al.* Aqueous phase phosphorescence: ambient triplet harvesting of purely organic phosphors via supramolecular scaffolding. *Angew. Chem. Int. Ed.* **130**, 17361-17365 (2018).
13. Zhou, B. & Yan, D. Hydrogen-bonded two-component ionic crystals showing enhanced long-lived room-temperature phosphorescence via TADF-assisted Förster resonance energy transfer. *Adv. Funct. Mater.* **29**, 1807599 (2019).
14. Kabe, R. & Adachi, C. Organic long persistent luminescence. *Nature* **550**, 384-387 (2017).

15. Li, D. *et al.* Amorphous metal-free room-temperature phosphorescent small molecules with multicolor photoluminescence via a host–guest and dual-emission strategy. *J. Am. Chem. Soc.* **140**, 1916-1923 (2018).
16. Wei, J. *et al.* Induction of strong long-lived room-temperature phosphorescence of N-phenyl-2-naphthylamine molecules by confinement in a crystalline dibromobiphenyl matrix. *Angew. Chem. Int. Ed.* **128**, 15818-15822 (2016).
17. Bolton, O., Lee, K., Kim, H. -J., Lin, K.Y. & Kim, J. Activating efficient phosphorescence from purely organic materials by crystal design. *Nat. Chem.* **3**, 205-210 (2011).
18. Tian, R., Xu, S. -M., Xu. Q. & Lu, C. Large-scale preparation for efficient polymer-based room-temperature phosphorescence via click chemistry. *Sci. Adv.* **6**, eaaz6107 (2020).
19. Su, Y. *et al.* Ultralong room temperature phosphorescence from amorphous organic materials toward confidential information encryption and decryption. *Sci. Adv.* **4**, eaas9732 (2018).
20. Zhang, G., Palmer, G. M., Dewhirst, M. W. & Fraser, C. L. A dual-emissive-materials design concept enables tumour hypoxia imaging. *Nat. Mater.* **8**, 747-751 (2009).
21. Yang, J. *et al.* Elucidating the excited state of mechanoluminescence in organic luminogens with room-temperature phosphorescence. *Angew. Chem. Int. Ed.* **129**, 15501-15505 (2017).
22. Huang, L. *et al.* Proton-activated “off–on” room-temperature phosphorescence from purely organic thioethers. *Angew. Chem. Int. Ed.* **130**, 16278-16282 (2018).
23. Chen, B., Zhang, X., Wang, Y., Miao, H. & Zhang, G. Aggregation-induced emission with long-lived room-temperature phosphorescence from methylene-linked organic donor–acceptor Structures. *Chem–Asian J.* **14**, 751-754 (2019).
24. Luo, J. *et al.* Aggregation-induced emission of 1-methyl-1, 2, 3, 4, 5-pentaphenylsilole. *Chem. Commun*. 1740-1741 (2001).

25. Guo J. *et al.* Achieving high-performance nondoped OLEDs with extremely small efficiency roll-off by combining aggregation-induced emission and thermally activated delayed fluorescence. *Adv. Funct. Mater.* **27**, 1606458 (2017).
26. Venkatramaiah, N., Kumar, G. D., Chandrasekaran, Y., Ganduri, R. & Patil S. Efficient blue and yellow organic light-emitting diodes enabled by aggregation-induced emission. *ACS Appl. Mater. Interfaces* **10**, 3838-3847 (2018).
27. Wong M. Y. & Zysman-Colman, E. Purely organic thermally activated delayed fluorescence materials for organic light-emitting diodes. *Adv. Mater.* **29**, 1605444 (2017).
28. Li, X., Jiang, M., Lam, J. W., Tang. B. Z & Qu, J. Y. Mitochondrial imaging with combined fluorescence and stimulated Raman scattering microscopy using a probe of the aggregation-induced emission characteristic. *J. Am. Chem. Soc.* **139**, 17022-17030 (2017).
29. Yuan, Y., Xu, S., Cheng, X., Cai, X. & Liu, B. Bioorthogonal turn-on probe based on aggregation-induced emission characteristics for cancer cell imaging and ablation. *Angew. Chem. Int. Ed.* **55**, 6457-6461 (2016).
30. Chen, J. *et al.* Amphiphilic polymer-mediated aggregation-induced emission nanoparticles for highly sensitive organophosphorus pesticide biosensing. *ACS Appl. Mater. Interfaces* **11**, 32689-32696 (2019).
31. Shi, Y. *et al.* Helical sulfono-γ-AApeptides with aggregation-induced emission and circularly polarized luminescence. *J. Am. Chem. Soc.* **141**, 12697-12706 (2019).
32. Shen, C. *et al.* Helicene-derived aggregation-induced emission conjugates with highly tunable circularly polarized luminescence. *Mater. Chem. Front.* **4**, 837-844 (2020).

33. Shyamal, M., Maity, S., Maity, A., Maity, R., Roy, S. & Misra, A. Aggregation induced emission based "turn-off" fluorescent chemosensor for selective and swift sensing of mercury (II) ions in water. *Sensor. Actuat. B-Chemical* **263**, 347-359 (2018).
34. Yu, Y. *et al.* Room-temperature-phosphorescence-based dissolved oxygen detection by core-shell polymer nanoparticles containing metal-free organic phosphors. *Angew. Chem. Int. Ed.* **56**, 16207-16211 (2017).
35. Su, Q., Lu, C. & Yang, X. Efficient room temperature phosphorescence carbon dots: Information encryption and dual-channel pH sensing. *Carbon* **152**, 609-615 (2019).
36. Louis, M., Thomas, H., Gmelch, M., Haft, A., Fries, F. & Reineke, S. Blue-light-absorbing thin films showing ultralong room-temperature phosphorescence. *Adv. Mater.* **31**, 1807887 (2019).
37. Tian, Z. *et al.* Multilevel data encryption using thermal-treatment controlled room temperature phosphorescence of carbon dot/polyvinylalcohol composites. *Adv. Sci.* **5**, 1800795 (2018).
38. Fateminia, S. A., Mao, Z., Xu, S., Yang, Z., Chi, Z. & Liu, B. Organic nanocrystals with bright red persistent room-temperature phosphorescence for biological applications. *Angew. Chem. Int. Ed.* **56**, 12160-12164 (2017).
39. He, Z. *et al.* Achieving persistent, efficient, and robust room-temperature phosphorescence from pure organics for versatile applications. *Adv. Mater.* **31**, 1807222 (2019).
40. Wang, T. *et al.* Aggregation-induced dual-phosphorescence from organic molecules for nondoped light-emitting diodes. *Adv. Mater.* **31**, 1904273 (2019).
41. Klimes, K., Zhu, Z. Q. & Li, J. Efficient blue phosphorescent OLEDs with improved stability and color purity through judicious triplet exciton management. *Adv. Funct. Mater.* **29**, 1903068 (2019).

42. Vydrov, O. A. & Scuseria, G. E. Assessment of a long-range corrected hybrid functional. *J. Chem. Phys.* **125**, 234109 (2006).

43. Tomasi, J., Mennucci, B. & Cammi, R. Quantum mechanical continuum solvation models. *Chem. Rev.* **105**, 2999-3094 (2005).

44. Lu, T. & Chen, F. Multiwfn: a multifunctional wavefunction analyzer. *J. Comput. Chem.* **33**, 580-592 (2012).

45. Hu, R. *et al.* Twisted intramolecular charge transfer and aggregation-induced emission of BODIPY derivatives. *J. Phys. Chem. C* **113**, 15845-15853 (2009).

46. Sun, Y. P., Sears Jr, D. F. & Saltiel, J. Resolution of benzophenone delayed fluorescence and phosphorescence spectra. Evidence of vibrationally unrelaxed prompt benzophenone fluorescence. *J. Am. Chem. Soc.* **111**, 706-711 (1989).

47. Nakayama, T., Sakurai, K., Hamanoue, K. & Otani, A. Effect of water on the phosphorescence spectra of aromatic carbonyl compounds. Part 2.—Dual phosphorescence of benzophenone at 77 K in ethanol–water. *J. Chem. Soc., Faraday Trans.* **87**, 1509-1512 (1991).

48. Klán, P., Wirz, J. *Photochemistry of organic compounds: from concepts to practice*. John Wiley & Sons (2009).

49. You, Y., Han, Y., Lee, Y. -M., Park, S. Y., Nam, W. & Lippard, S. J. Phosphorescent sensor for robust quantification of copper (II) ion. *J. Am. Chem. Soc.* **133**, 11488-11491 (2011).

50. Zhang, K. Y. *et al.* Dual-phosphorescent iridium (III) complexes extending oxygen sensing from hypoxia to hyperoxia. *J. Am. Chem. Soc.* **140**, 7827-7834 (2018).

51. Dolomanov, O. V., Bourhis, L. J., Gildea, R. J., Howard, J. A. & Puschmann, H. OLEX2: a complete structure solution, refinement and analysis program. *J. Appl. Crystallogr.* **42**, 339-341 (2009).

52. Sheldrick, G. M. SHELXT–Integrated space-group and crystal-structure determination. *Acta Crystallogr. A* **71**, 3-8 (2015).